Seismic monitoring short-duration events: liquefaction in 1*g* models

Jong-Sub Lee and J. Carlos Santamarina

Abstract: The duration of liquefaction in small models is very short, therefore special monitoring systems are required. In an exploratory sequence of liquefaction tests, S-wave transillumination is implemented with a high repetition rate to provide detailed information on the evolution of shear stiffness during liquefaction. These data are complemented with measurements of acceleration, time-varying settlement, excess pore pressure, and resistivity profiles. Measurements show that excess pore pressure migration from liquefied deep layers may cause or sustain a zero effective stress condition in shallow layers, that multiple liquefaction events may take place in a given formation for a given excitation level, and that unsaturated layers may also reach a zero effective stress condition. The time scale for excess pore pressure dissipation in fully submerged specimens is related to particle resedimentation and pressure diffusion; downward drainage from unsaturated shallow layers may contribute an additional time scale. High resolution resistivity profiling reveals the gradual homogenization of the soil bed that takes place during subsequent liquefaction events. The S-wave transillumination technique can be extended to field applications and implemented with tomographic coverage to gain a comprehensive understanding of the spatial and temporal evolution of liquefaction.

Key words: densification, electrical resistivity, multiple liquefaction, pore pressure, shear wave, spatial variability.

Résumé : La durée de la liquéfaction dans de petits modèles est très courte; en conséquence, des systèmes spéciaux de mesures sont requis. Dans une séquence exploratoire d'essais de liquéfaction, on a mis en place une transillumination d'ondes *S* avec un taux de répétition élevé pour fournir une information détaillée sur l'évolution de la rigidité en cisaillement durant la liquéfaction. Ces données sont complétées par des mesures de l'accélération, du tassement variant en fonction du temps, de l'excédent de la pression interstitielle, et des profils de résistivité. On a répété les essais sous différentes conditions de saturation. Bien que l'étude soit restreinte par les limitations inhérentes à la faible dimension des modèles de 1*g*, on s'attend à ce que plusieurs informations soient valables pour des échelles plus grandes. Des mesures montrent que la migration de l'excédent de pression interstitielle des couches profondes liquéfiées peuvent causer ou soutenir une condition de contrainte effective nulle dans les couches peu profondes, que des événements de liquéfaction multiples peuvent se produire dans une formation donnée à un niveau d'excitation donné, et que les couches non saturées peuvent aussi atteindre une condition de contrainte effective nulle. L'échelle de temps pour la dissipation de l'excédent de la pression interstitielle dans des spécimens complètement submergés est en relation avec la resédimentation des particules et la diffusion de la pression; le drainage vers le bas des couches peu profondes non saturées peuvent contribuer à une durée additionnelle. Bien que l'évolution de la propagation de la vitesse et de l'atténuation de l'onde de cisaillement varient en parallèle avec l'histoire de la durée de l'excédent de la pression durant un événement, un profilage de résistivité à hauite résolution documente l'homogénéisation graduelle du lit de sol qui se produit durant les événements subséquents de liquéfaction. La technique de transillumination de l'onde *S* peut être élargie à des applications sur le terrain et utilisée avec une couverture tomographique pour acquérir une compréhension complète de l'évolution spatiale et temporelle de la liquéfaction.

Mots-clés : densification, résistivité électrique, liquéfaction multiple, pression interstitielle, onde de cisaillement, variabilité spatiale.

[Traduit par la Rédaction]

Introduction

Monotonic, cyclic, or combined undrained loading may cause excess pore-water pressure generation; eventually, the effective stress may decrease to zero and initial liquefaction is attained (Seed 1979; Alarcon-Guzman et al. 1988; Ishihara 1996; Youd et al. 2001). Flow liquefaction occurs when the post-liquefaction shear strength is lower than the initial deviatoric stress acting at the site, and it is accompanied by sudden large lateral deformation, for example, sloping ground.

Received 10 August 2004. Accepted 8 August 2006. Published on the NRC Research Press Web site at cgj.nrc.ca on 18 July 2007.

J.S. Lee. Civil and Environmental Engineering, Korea University, Seoul 136-701, Korea.
J.C. Santamarina.[1] Civil and Environmental Engineering, Georgia Institute of Technology, Atlanta, GA 30332, USA.

[1]Corresponding author (e-mail: carlos.santamarina@ce.gatech.edu).

 doi:10.1139/T07-020

Fig. 1. Liquefaction tank and instrumentation. Notation: subindices T, M, and B indicate top, middle and bottom positions; A, accelerometer (horizontal axis); P, pore pressure transducer; S and R, source and receiver bender elements. Saturation conditions: C1, fully submerged; C2, unsaturated upper part by water table drawdown; and C3, unsaturated upper part by capillary rise. The average degree of saturation in the upper part of specimen C2 is S = 87% (probably convex trend), while the average degree of saturation in the upper part of specimen C3 is S = 82% (probably concave trend).

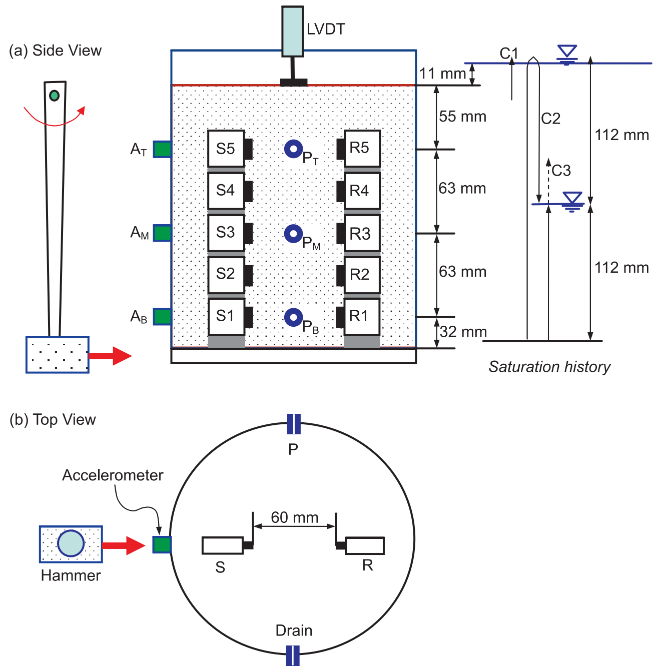

Fig. 2. Typical acceleration response measured with the three accelerometers after a single impact.

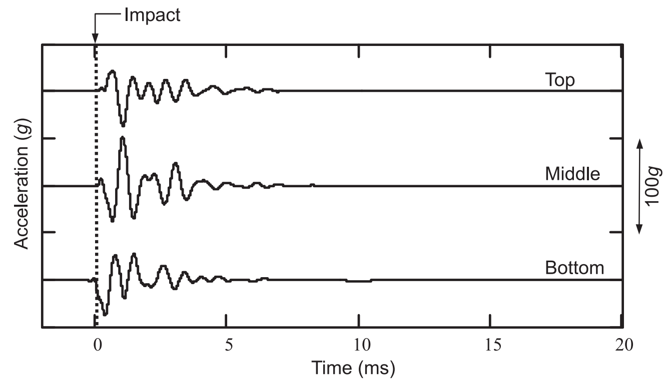

On the other hand, cyclic mobility refers to the incremental weakening of soils during cyclic loading when the initial static shear stress is lower than the monotonic shear strength on the critical state line, for example, level ground subjected to a seismic event (Krammer 1996; Vaid and Sivathayalan 2000). This study explores zero effective stress conditions generated by short transient excitations, herein referred to simply as liquefaction.

The study of liquefaction has involved small specimens in laboratory cells (e.g., cyclic triaxial tests; Seed and Lee 1966), small scale model tests in centrifuges and at 1*g* (Schofield 1981; Arulanandan and Scott 1993; Kokusho 1999; Park 2001), and artificially generated events in the field (e.g., Florin and Ivanov 1961; Ashford et al. 2004). More recently, instruments have been installed in the field to monitor real events, such as in the Wildlife site in the USA (Youd and Holzer 1994), near Lotung, Taiwan (Tang 1987; Zeghal et al. 1995), and in Sunamachi, Japan (Ishihara et al. 1989).

Instrumenting a soil mass to study liquefaction presents various challenges, including the effect of transducer installation on the soil response. The propagation of small-strain shear waves does not affect the ongoing process. Furthermore, while instruments such as accelerometers or pore pressure transducers are point measurements, the propagation of shear waves from a source to a receiver is a boundary-based measurement that can be inverted to generate a tomographic image. Shear wave propagation depends on the state of effective stress in freshly remolded uncemented soils when capillary effects are negligible; in this case, the shear wave velocity is related to the effective stresses acting in the direction of wave propagation and in the direction of particle motion (Roesler 1979; Knox et al. 1982; Yu and Richart 1984).

The purpose of this study is to explore the implementation of shear wave based monitoring of liquefaction events. The project was commissioned under the National Science Foundation – Network for Earthquake Engineering Simulation (NSF–NEES), with application in the University of California at Davis centrifuge. The short-duration of liquefaction in small-scale models adds significant challenges to this development. The system as it was designed and built is described next. Then, results from a validation study with 1*g* models at varying saturation conditions are presented. Time-varying shear wave velocity and amplitude measurements are complemented with settlement, acceleration, pore pressure, and elegctrical resistance measurements.

S-wave systems for short-duration events

The duration of a liquefaction event can be estimated from the resulting volume change in the soil mass, $[H\Delta e/(1+e_o)]$, and the flow rate, $ki_{cr} = k\rho'/\rho_w$, in terms of the initial void ratio e_o, the void ratio change Δe, the critical hydraulic gradient i_{cr}, the mass density of water ρ_w, the submerged density of the soil ρ', the soil column height H, and its permeability k. Then, the time scale for the duration of the liquefaction event is predicted to be (see also Scott 1986; Kokusho 2003)

$$[1] \qquad t = \frac{\Delta e}{1+e_o}\frac{\rho_w}{\rho'}\frac{H}{k}$$

For example, for a small-scale model, H = 0.5 m, e_o = 0.7, Δe = 0.02, and k = 0.01 cm/s, the duration of liquefaction is $t \approx 60$ s.

The spatial evolution of liquefaction can be monitored with S-wave tomographic techniques. However, gathering tomographic data for such a short-duration event is challenging and faces significant difficulties with noise control. Instead, a new technique based on continuous transillumination measurements is developed herein. The hardware consists of two columns of five bender elements each, mounted in a crosshole configuration as shown in Fig. 1. The directions of

Fig. 3. Cumulative settlement time histories shown after selected impacts. (*a*) Fully submerged C1 specimen. (*b*) Mixed saturation C2 specimen.

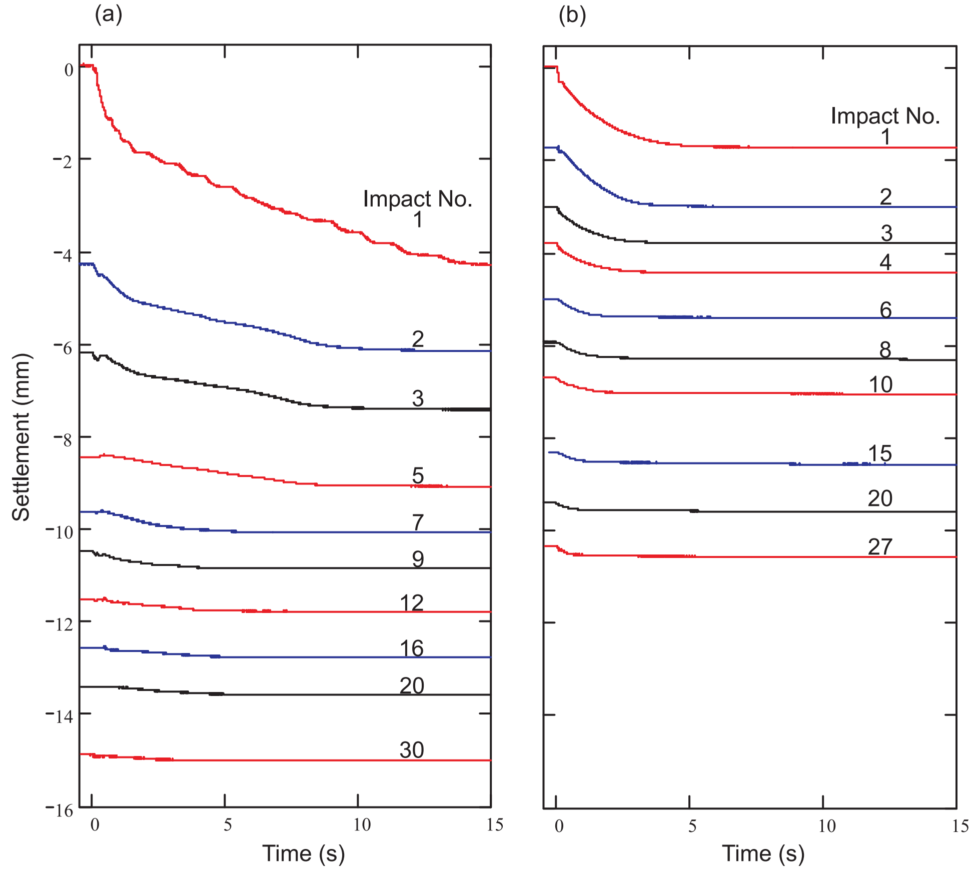

Fig. 4. Settlement versus impact number. Note that the mixed saturation C2 specimen has higher initial saturation in the upper part than the mixed saturation C3 specimen.

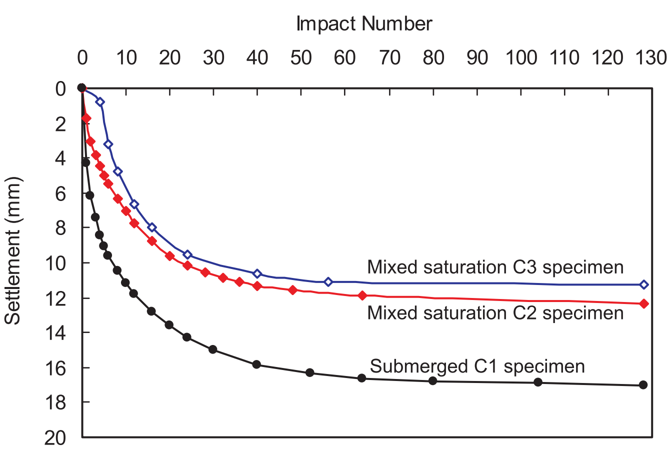

Fig. 5. Average void ratio versus impact number for the fully submerged C1 specimen. The critical state void ratio at σ′ = 1 kPa is $e_{cs} \approx 0.91$.

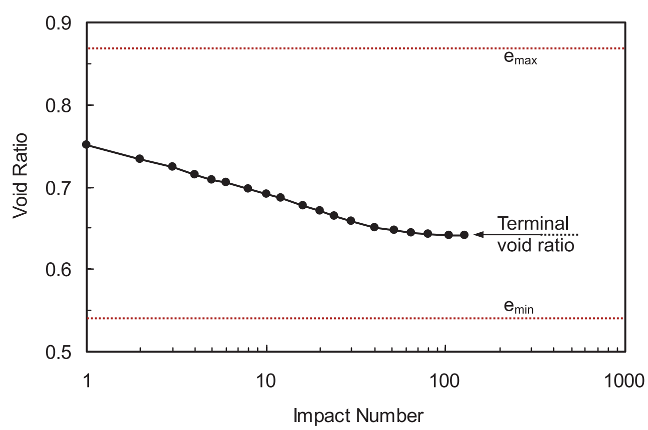

wave propagation and of particle motion are both on the horizontal plane. The tip-to-tip crosshole distance between the source and the receiver bender elements is 60 mm. A plane wave is generated by feeding a square-tooth input signal (frequency, $f \approx 65$ Hz) simultaneously to all bender elements on one side (S1 through S5 in Fig. 1). The continuous signal detected at each of the bender elements on the other side (R1 through R5 in Fig. 1) is recorded without interruption for ~1.6 s, with a sampling frequency 20 kHz so that each stored signal includes 32 000 discrete values. Each cycle of the square-tooth input signal produces two events 7.7 ms apart, and a total of ~210 events are detected in the signal recorded at each elevation.

There is no time for signal stacking in one-of-a-kind short-duration liquefaction events. Signal processing procedures developed for noise control and data reduction in this

Fig. 6. Electrical resistivity profiles after preparation and after different impacts. (*a*) Fully submerged C1 specimen. (*b*) Mixed saturation C2 specimen. Note that 0* indicates during specimen preparation.

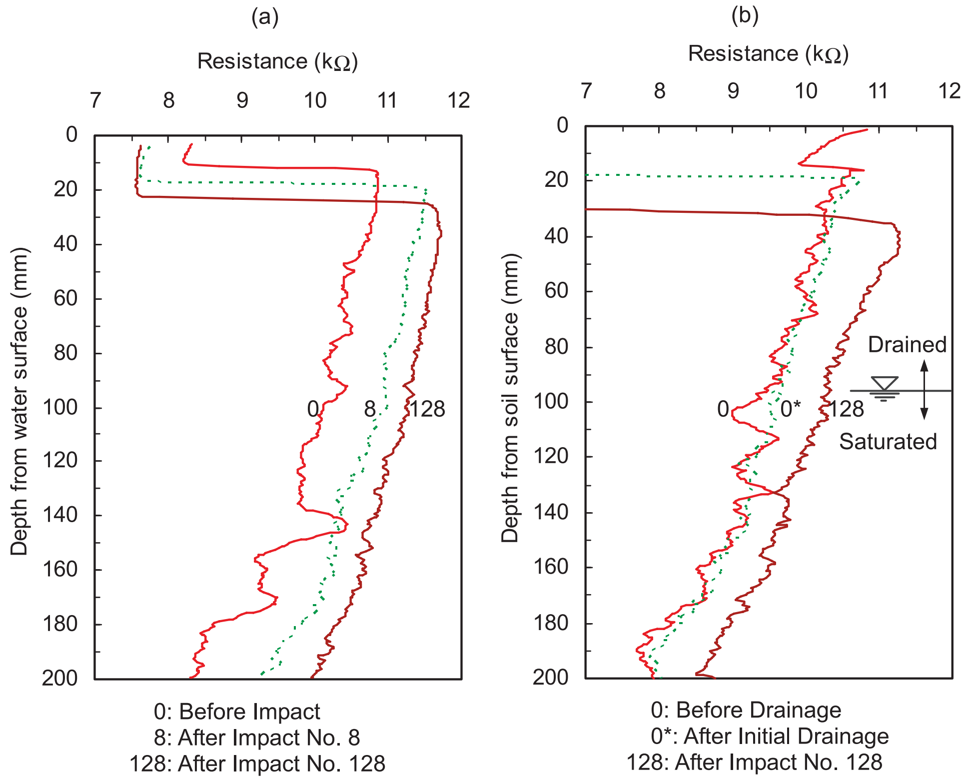

application are based on frequency domain filtering (high pass ≈ 500 Hz) and a time-moving cross correlation analysis for the determination of the travel time and amplitude of each detected event. The cross correlation is implemented between the first signal measured before liquefaction and all other signals measured with the same bender element.

Experimental design

The S-wave transillumination tool is assessed herein using a one-dimensional liquefaction tank at 1*g*. Different saturation conditions are explored as part of this study. Test procedures and complementary measurement systems are described next (see Lee 2003 for a complete dataset).

Liquefaction tank, soil, and specimen preparation

Nevada sand is used for this study (mean particle diameter D_{50} = 0.16 mm, coefficient of uniformity C_u = 1.62, coefficient of curvature C_c = 1.26, Unified Classification System: SP; maximum void ratio e_{max} = 0.87, minimum void ratio e_{min} = 0.54; critical state void ratio at 1 kPa, $e_{1kPa} \approx 0.91$). It is placed in an acrylic cylinder as sketched in Fig. 1 (190 mm inner diameter and 270 mm height). Multiple liquefaction events are induced in three specimens with different saturation conditions: fully submerged specimen (C1) and two mixed saturation specimens, which are partially saturated in the upper part and fully saturated in the lower part (cases C2 and C3).

The sand deposit in the fully submerged specimen (C1) is prepared using the water pluviation technique. The sand is continuously rained while maintaining a constant water height above the sand bed. At the end of pluviation, the thickness of the sand layer is 213 mm, and the free water surface is 11 mm above the sand surface. The mean initial void ratio is e_o = 0.79.

The mixed saturation specimen case C2 is prepared under submerged conditions (identical to specimen case C1 with e_o = 0.79). Then, drainage is allowed until the water table reaches the middle height of the tank, leaving a partially saturated specimen in the upper half (all dimensions are specified in Fig. 1). The lower half of the second mixed saturation specimen, case C3, is prepared under submerged conditions; then, the water table is lowered to the surface of the sand bed, the upper layer is placed using the dry pluviation method, and water is allowed to ascend into the upper layer by capillarity (the mean initial void ratio is e_o = 0.81). The location of the drainage port is the same in cases C2 and C3 (Fig. 1). A specimen with higher saturation is obtained in case C2 than in case C3 due to hysteresis in capillarity.

Measurement system

The tank is impacted at the base using a 4.4 N and 540 mm long pendulum that is released from a 35° initial angle. During and after the impact, the soil response is assessed using the S-wave transillumination and various complementary devices (see Fig. 1). Three accelerometers (PCB: 352B65, Depew, N.Y.) capture the motion of the tank at three levels. An LVDT is used to measure the surface settlement during liquefaction (Collins Technologies: SS-107, Long Beach, Calif.), and three transparent scales attached on

Fig. 7. Evolution of pore pressure head ($h = u/\rho_w g$ where u is pore pressure, ρ_w is density of water, and g is the acceleration of gravity) versus time after different impacts in the fully submerged C1 specimen. Note that $h_o = z_w$, $h_e^{max} = z_w + z_s(\rho_{sat} - \rho_w)/\rho_w$ (z_w and z_s are water and soil depth). Numbers in circles denote impact number.

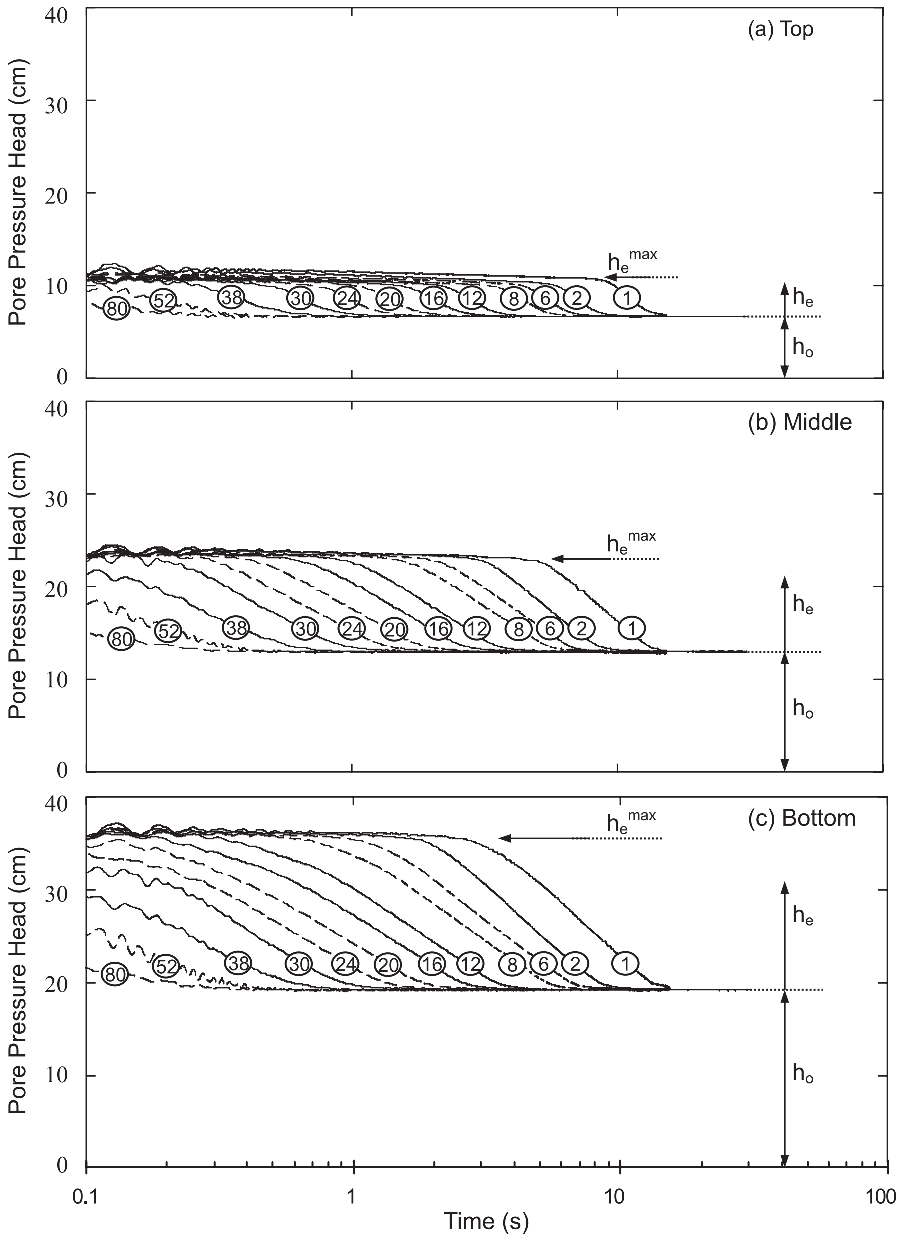

the wall of the tank permit corroboration of the surface settlement after each impact. An electrical resistance needle probe is inserted at selected times to determine electrical resistivity profiles (implementation details in Cho et al. 2004). Finally, three pore pressure transducers (OMEGA: 163PC01D48, Stamford, Conn.) installed at the same elevations as the accelerometers yield changes in pore-water pressure during liquefaction.

Comments on scale models

Shear-induced liquefaction in the field typically happens at a depth of 2–10 m from the soil surface (Youd and Bennett 1983; Zeghal and Elgamal 1994; Kokusho 2003). This depth reflects a compromise between the stress- and strain-dependent contractive tendency of a soil and the imposed strain level (the strain level decreases with depth during a seismic event and eventually falls bellow the elastic threshold strain). Scaled model tests at 1g are subjected to low stress levels, therefore, high initial void ratios are required to attain liquefaction. Scale model tests, both 1g and Ng, also face difficulties associated with soil structure, boundary effects, and grain-size effects (Rocha 1957; Iai 1989; Poorooshasb 1995; Gibson 1997). Nevertheless, events in small-scale models are physical realities that can provide valuable insight when properly analyzed (Iai 1989; Gibson 1997; Kokusho 1999; Park 2001).

Fig. 8. Evolution of pore pressure head ($u/\rho_w g$) versus time after different impacts in the mixed saturation C2 specimen. Note that $h_o = z_w$, $h_e^{max} = z_w + z_s(\rho_{sat} - \rho_w)/\rho_w$, ($z_w$ and z_s are water and soil depth). Numbers in circles denote impact number.

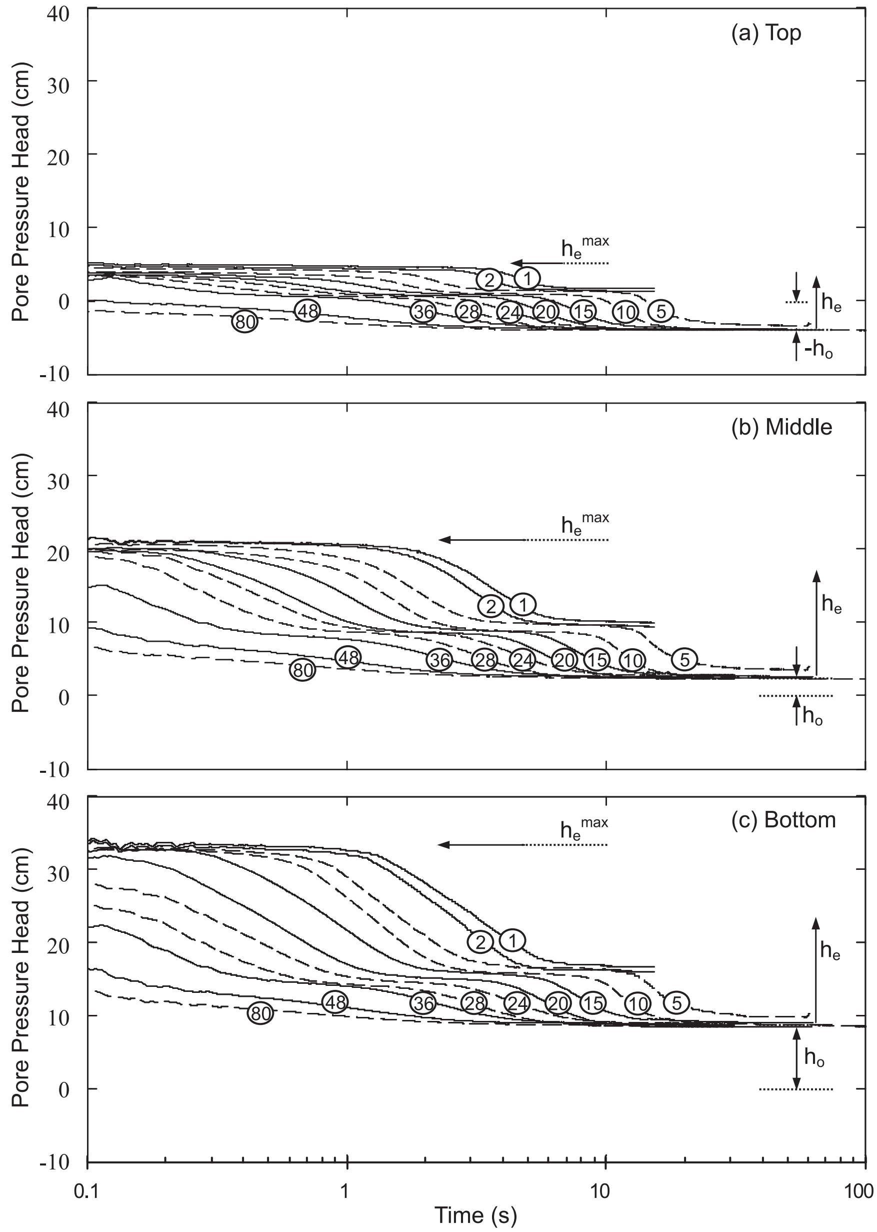

Results

The three models prepared with different saturation conditions (cases C1, C2, and C3) are subjected to multiple induced vibrations. Full excess pore pressure dissipation and complete settlement are confirmed before each successive impact (typically 2 min between impacts). The acceleration, settlement, electrical resistance, pore pressure, and shear wave velocity and amplitude are measured during every vibration event. Results are presented next.

Acceleration response

The typical acceleration time series measured at the three different elevations on the tank wall after a single impact are plotted in Fig. 2. The peak horizontal acceleration ranges between 38g and 53g (see Kokusho 1999 for similar results). The spectral density shows that most of the energy is between 800 and 1800 Hz (predominant frequency ≈ 1000 Hz). A time delay of ~0.5 ms is observed between subsequent accelerometers (i.e., approximately a π-shift). The system attenuation is high (damping ratio ≈ 10%), and the tank vibration ends before ~6 ms.

Settlement

The measured cumulative surface settlements versus time are presented in Fig. 3 for the fully submerged specimen C1 and the mixed saturation C2 specimen (data are shown for selected impacts). Trends are similar: the incremental settle-

Fig. 9. Excess pore pressure generation: impact number versus soil depth. Full excess pore pressure generation stops developing after a relatively large number of impacts.

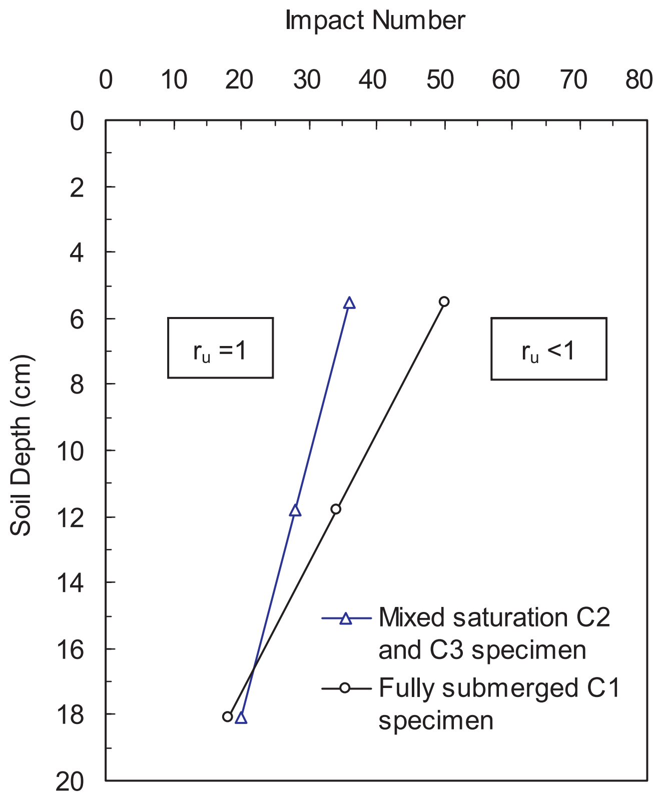

ment at the end of each liquefaction event and the settlement duration decrease with successive impacts.

Figure 4 shows the measured cumulative settlement versus impact number trends for the three specimens. The settlement after each event decreases with successive impacts in all models. Notice the delayed settlement in the mixed saturation C3 specimen given its lower initial saturation (water does not exit the drainage port until the fourth impact; hence, saturation increases by densification before water is released from the soil matrix). Regenerated capillary suction after drainage hinders soil settlement in the mixed saturation specimens, and smaller settlements are measured in mixed saturation specimens.

Figure 5 shows the average void ratio after each impact in the fully submerged specimen: the void ratio decreases linearly with impact number until "the terminal void ratio" $e_{term} \approx 0.64$ is reached. The relative density at this void ratio is $D_r \approx 70\%$.

Electrical resistivity profiles

Soil porosity profiles before and after impact are obtained using the electrical needle probe tests. Test results in the fully submerged C1 specimen are plotted in Fig. 6*a*. The electrical resistivity increases with the number of impacts due to the decrease in porosity. The electrical resistivity measured before impact shows several humps suggesting initial density variations (e.g., at depths of 70 mm, 92 mm, 144 mm, and 170 mm). These humps rapidly disappear, and they are not detected after the eighth impact. Therefore, densification is accompanied by vertical homogenization (refer to Fig. 3). The electrical resistivity profiles gathered in the mixed saturation C2 specimen are plotted in Fig. 6*b*. The plotted data include profiles before and after the initial drainage during specimen preparation, and after 128 impacts. Once again, a clear shift in electrical resistivity is observed after 128 impacts due to the decrease in porosity. Similar results are observed in the mixed saturation C3 specimen (not shown).

The decrease in electrical resistance with depth observed in Figs. 6*a* and 6*b* reflects inevitable size segregation in water-pluviated Nevada sand (Stokes law). In contrast, electrical resistance is quasiconstant with depth in specimens prepared with clean uniform sand (Cho et al. 2004).

Pore pressure

The pore pressure head versus time response measured at the three different levels in the fully submerged C1 specimen and the mixed saturation C2 specimen are plotted in Figs. 7 and 8 for selected impacts. Trends are similar for the two mixed saturation specimens. The pore pressure dissipation signatures gathered from the submerged C1 specimen are different from those gathered from the mixed saturation C2 specimen.

Pore pressure dissipation shows two stages in the fully submerged C1 specimen in Fig. 7. In the first stage, the excess pore pressure remains constant; in the second stage, the excess pore pressure dissipates and converges asymptotically to zero excess pore pressure ($u_e = 0$). The ratio r_u between the excess pore pressure and the initial vertical effective stress is $r_u = 1$ in the first stage, indicating liquefied conditions. As the impact number increases, the duration of the first stage decreases and it eventually disappears; thus, full liquefaction stops developing after a large number of similar impacts.

Pore pressure dissipation shows two stages of constant head in the mixed saturation C2 specimen (Fig. 8). These two stages and their associated time scales are related to the drainage time for water percolating downwards from the unsaturated region, and flowing upwards as the saturated lower sand resediments after the liquefaction event.

The solidification front moves from the bottom up. Until the solidification front reaches depth z, the excess pore pressure ratio is $r_u = 1$, and the soil mass remains under zero effective stress at depth z. Full excess pore pressure $r_u = 1$ is attained at the bottom of the fully submerged C1 specimen even after the 20th impact (Fig. 7). Afterwards, the peak value is $r_u < 1$ and soil particles do not become completely suspended at the bottom of the specimen. Yet, the peak excess pore pressure ratio reaches $r_u = 1$ even after 34 and 50 impacts in the middle and near the top of the specimen, respectively. Similar trends are observed in the mixed saturation specimens (cases C2 and C3). Figure 9 shows the boundary for full excess pore pressure generation ($r_u = 1$) in terms of depth versus impact number. The boundary decreases linearly with depth indicating that the bottom layer stops generating full excess pore pressure before the upper layers. Significant r_u values are measured even after 80 impacts.

Fig. 10. Snapshots of the signal registered with the bender element (R1) after a single impact. The complete signal lasts 1600 ms and includes ~210 shear wave propagation events (fully submerged C1 specimen; impact No.: 24).

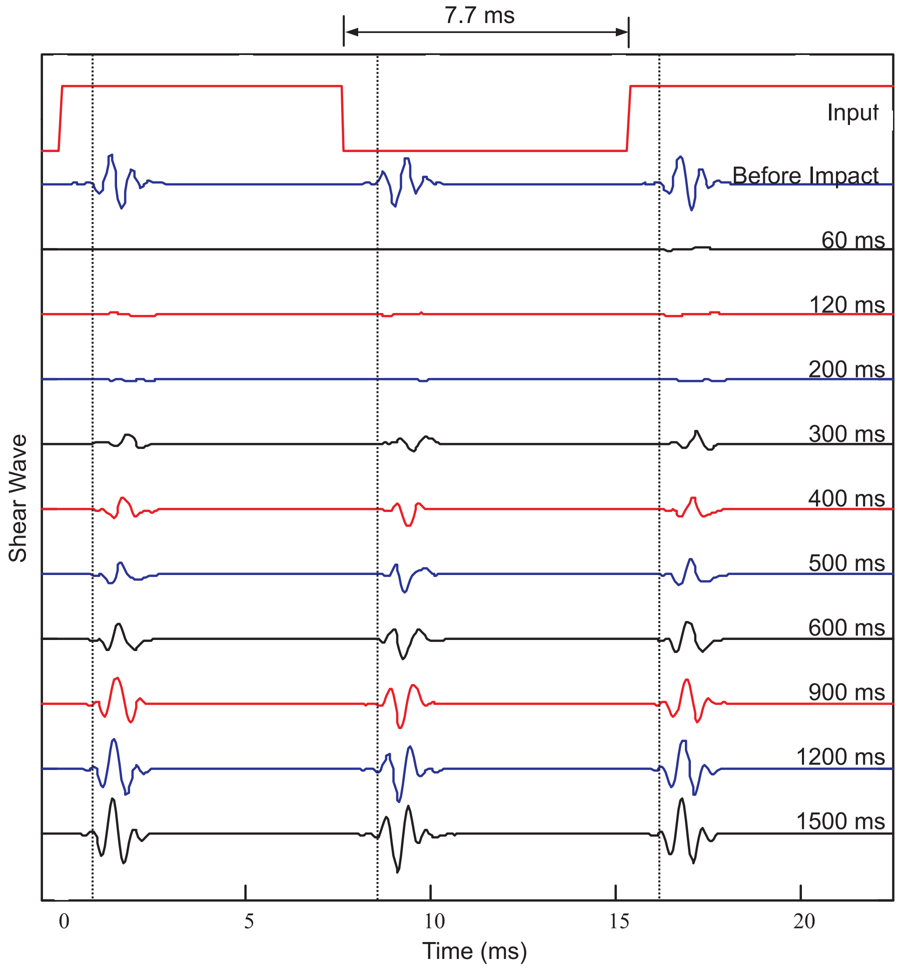

Shear wave

Shear wave propagation after a single impact

The signal gathered with a bender element after each impact captures ~210 shear wave propagation events during its ~1.6 s duration. Snapshots of a signal detected with the bottom bender are presented in Fig. 10. The shear wave initially disappears after the impact and gradually recovers afterwards; the travel time shortens and the signal amplitude increases with time.

The evolution of the shear wave velocity and amplitude with time for the fully submerged C1 specimen and the mixed saturation C2 specimen are plotted in Figs. 11 and 12. The S-wave signal is nil while r_u values are high; therefore arrival times cannot be detected and velocity values are not reported. On the other hand, the peak amplitude of the cross-correlation is properly computed at all times, and all values are reported. Note that travel time and amplitude recover faster at the bottom layer than at the top in the fully submerged specimen; this confirms the upward migration of the solidification front. Trends in shear wave velocity and amplitude versus time in the mixed saturation specimens (cases C2 and C3) are similar to those observed in the fully submerged C1 specimen.

Shear wave propagation with successive impacts

The value of shear wave velocity, V_S, after excess pore pressure dissipation is plotted versus impact number in Fig. 13. The S-wave velocity is higher for deeper measurements because of the higher mean effective stress on the polarization plane. In this installation, particle motion direction (⊥) and wave propagation direction (||) are on the horizontal plane, therefore (Knox et al. 1982)

$$[2] \qquad V_s = \alpha\left(\frac{\sigma'_\perp + \sigma'_\parallel}{2\,\text{kPa}}\right)^\beta = \alpha\left(\frac{\sigma'_h + \sigma'_h}{2\,\text{kPa}}\right)^\beta = \alpha\left(\frac{K_o\sigma'_v}{\text{kPa}}\right)^\beta$$

where K_o, the coefficient of earth pressure at rest, relates the horizontal effective stress σ'_h to the vertical effective stress σ'_v, and parameters α and β are experimentally determined. The α-coefficient and the β-exponent are interrelated as $\beta = 0.36 - \alpha/700$ (Santamarina et al. 2001). General guidelines for the value of β are: $\beta = 0.16$–0.20 for round sand particles, $\beta \approx 0.20$–0.25 for angular sands (lower values correspond to denser sands), $\beta \geq 0.25$ for soft clays, and $\beta \leq 0.15$ for overconsolidated clays and cemented soils.

The shear wave velocity increases with increasing impact number. A 16%–21% increase in V_S after the 128 impacts can be justified by the decrease in void ratio. However, the

Fig. 11. Evolution of shear wave with time for fully submerged C1 specimen; impact No. 24. (*a*) Shear wave velocity. (*b*) Cross-correlation amplitude.

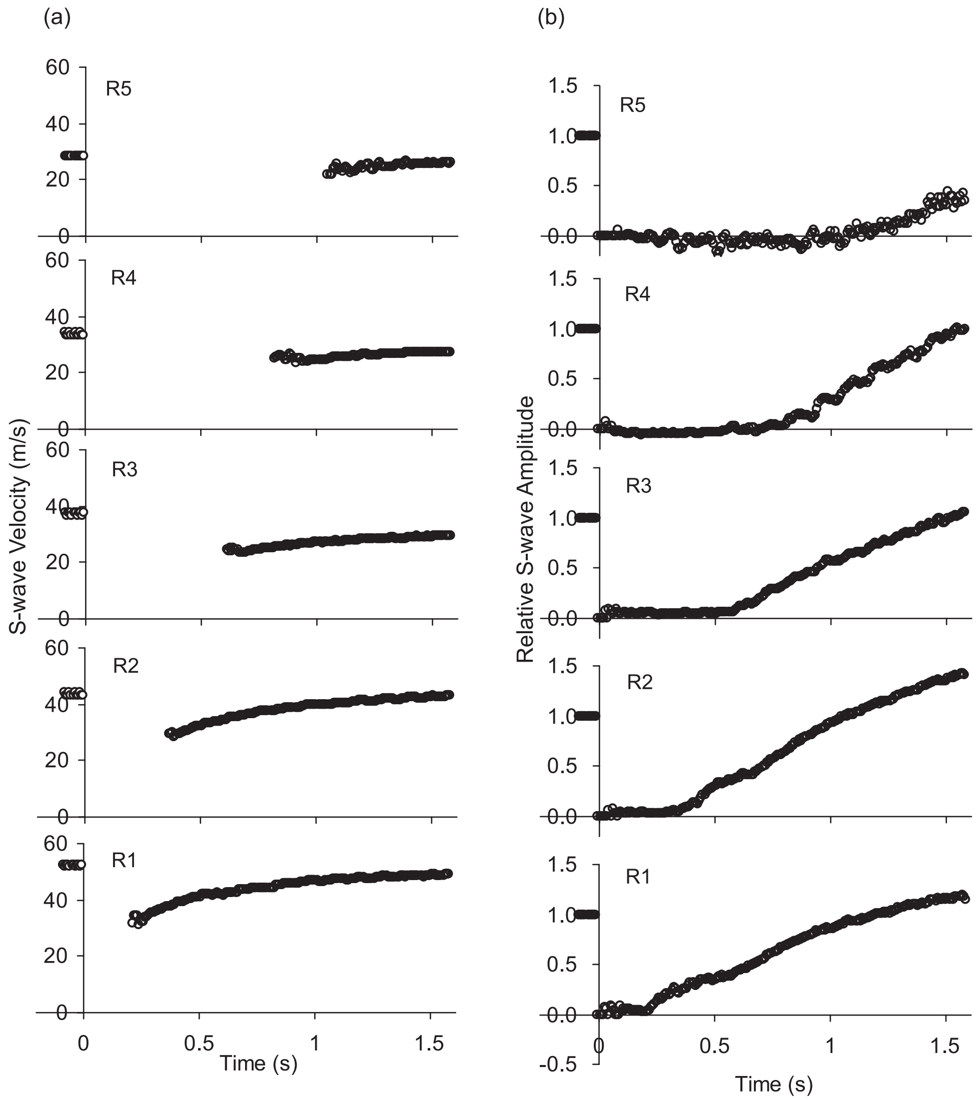

observed increase in shear wave velocity exceeds 50%~70% and implies an increase in horizontal effective stress (eq. [2]). The inferred increase in σ'_h may be a consequence of boundary conditions and excitation mode in this model study, and it may not necessarily take place under field conditions.

Wave transmission is facilitated in the unsaturated zone due to interparticle capillary forces. Therefore, the measured shear wave velocity reflects the combined effects of effective confinement and capillarity (Fig. 13*b*).

Analyses and discussion

Strain $\gamma = \partial\delta/\partial x$ and acceleration $\partial^2\delta/\partial t^2$ are related for a harmonic particle motion $\delta = Ae^{j(\omega t - \kappa x)}$ with displacement amplitude A, angular frequency $\omega = 2\pi f$, and spatial frequency $\kappa = 2\pi/\lambda$. Thus, the maximum shear strain is $\gamma_{max} = a_{max}\kappa/\omega^2 = a_{max}/2\pi f V_S$, where the peak acceleration is $a_{max} = A\omega^2$. The shear strain must exceed the threshold strain $\gamma_{max} > \gamma_{th}$ to cause excess pore pressure generation. Therefore, the required acceleration must be

$$[3] \qquad a_{trig} > \gamma_{th} 2\pi f V_S$$

Indeed, high acceleration is required to trigger excess pore pressure generation when high frequency excitation is used in scaled models, as compared to field situations. Data from reported cases confirm this observation: $a = 270g$ at $f = 3$ kHz (model impact, Kokusho 1999), $a = 53g$ at $f = 1$ kHz (this model study), $a = 0.25g$ at $f = 4$ Hz (shake table, low V_S; Park 2001), and $f = 0.7$ Hz at $a = 0.2g$ (Wildlife liquefaction array; Youd and Holzer 1994).

Excess pore pressure response and instantaneous propagation parameters

The excess pore pressure response and the evolution of S-wave velocity and amplitude are compared in Fig. 14 for impact Nos. 8 and 40 at the bottom of the fully submerged C1 specimen. Two independent time scales are apparent: the duration of imposed vibration (~6 ms) and the much longer

Fig. 12. Evolution of shear wave with time for mixed saturation C2 specimen; impact No. 24. (*a*) Shear wave velocity. (*b*) Cross-correlation amplitude.

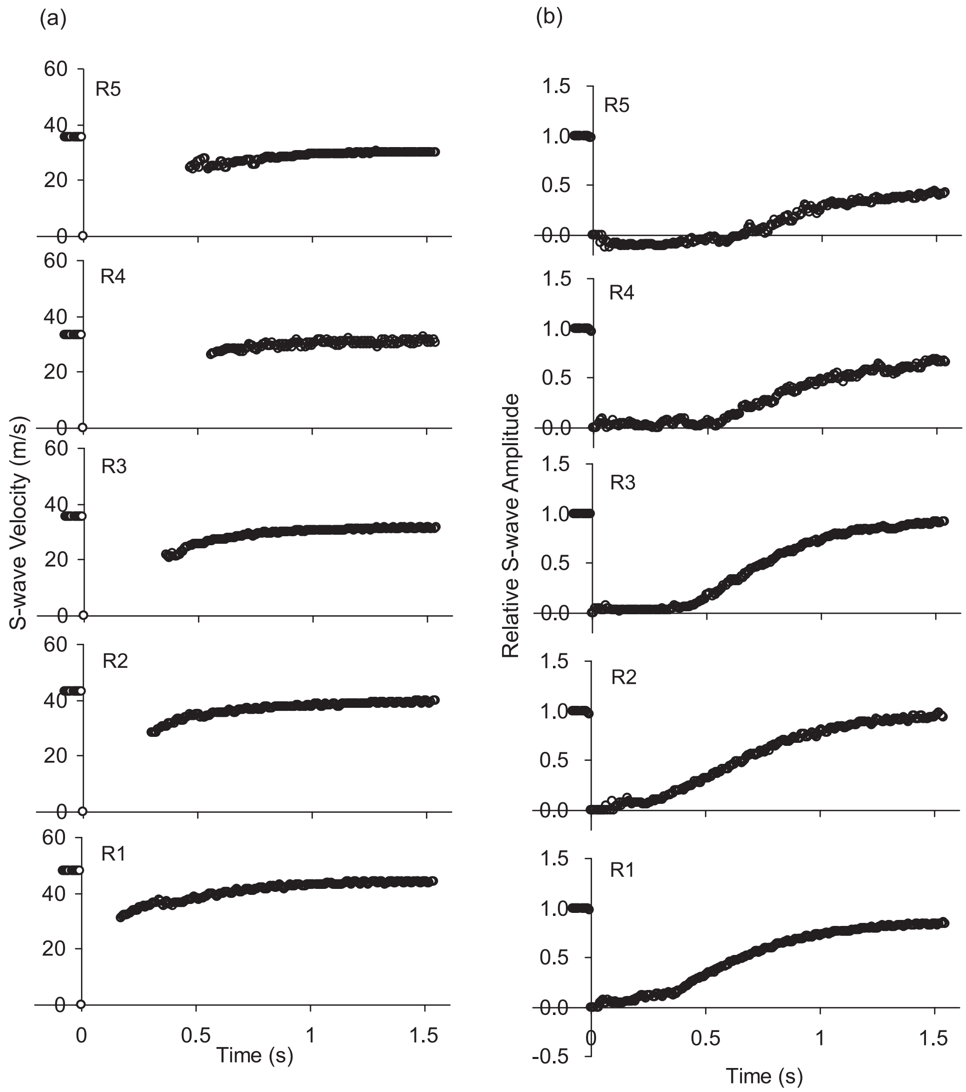

duration of excess pore pressure dissipation. While the global vibration quickly fades away, the excess pore pressure remains and may even increase after the acceleration has ended. Similar results have been obtained from field measurements at the Wildlife liquefaction site (Youd and Holzer 1994) and from centrifuge model tests with Nevada sand (Fiegel and Kutter 1994; Adalier and Elgamal 2002).

The evolution of shear wave velocity and amplitude parallels the generation and dissipation of excess pore pressure, indicating that better contact conditions favor stiffness and reduce energy loss during wave propagation. Wave propagation data gathered during isotropic loading and unloading of lead shot show that velocity depends on contact flatness while amplitude depends on contact force (Cascante and Santamarina 1996). Both contact flatness and contact forces are determined by the effective stress, and both instantaneous velocity and amplitude are correlated.

The r_u value is not constant when S-wave signals are detected first; for example (applies to one event): detection takes place at the bottom when r_u = 89%, at the middle when r_u = 52%, and at the top when r_u = 39%. The explanation involves the following observations: (*i*) the detection of shear wave signals requires a minimum effective stress; (*ii*) therefore, the solidification front must be a distance Δ above the elevation z of a source-receiver pair; and (*iii*) the corresponding r_u value for S-wave detection is $r_u = 1 - (\Delta/z)$. Therefore, the closer to the surface, the smaller z is and the lower r_u will be, as observed in the data. Note that the longer the distance between the source and the receiver, for example, in field applications, the higher the effective stress must be to attain adequate detection.

Liquefaction in unsaturated layers

Liquefaction resistance is expected to increase in unsaturated sands (Ishihara et al. 1998). Yet, liquefaction may still develop due to volume collapse, or due to the rapid upward transmission of excess pore pressure generated in deeper

Fig. 13. Shear wave velocity after complete pore-water pressure dissipation versus impact number. (*a*) Fully submerged C1 specimen. (*b*) Mixed saturation C2 specimen.

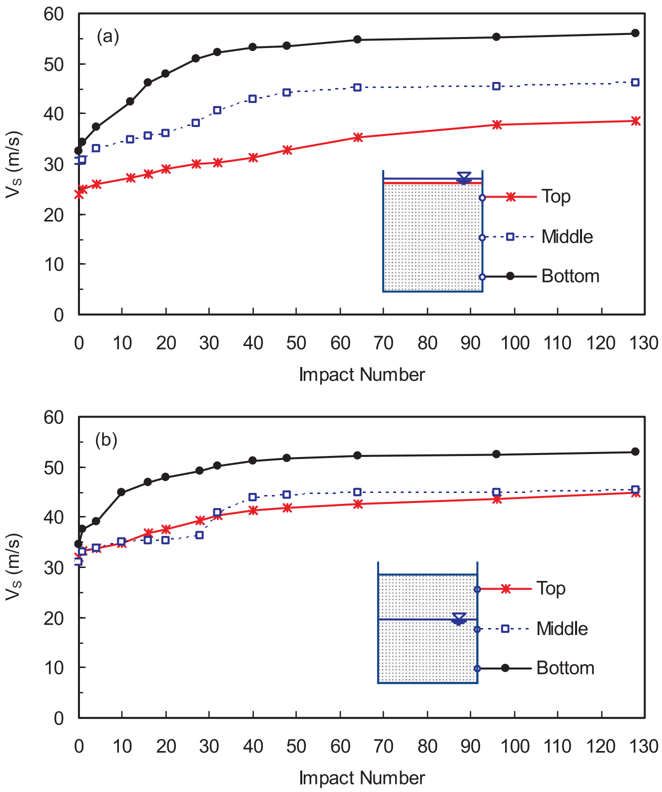

layers. The whole soil column experiences full excess pore pressure generation in the mixed saturated C2 specimen (see Fig. 8), and free water appears on the soil surface after each event, until the ~45th impact (free water appears in the C3 specimen after the first four impacts only; this model has lower saturation).

Solidification front

The liquefied soil mass is made up of suspended particles. The soil skeleton regenerates from the bottom of the specimen. Furthermore, the upward flow of water that dissipates from lower liquefied layers either triggers and (or) sustains the zero effective stress condition in the upper shallow layers (see also Schofield 1981).

The start time t_1 and the end time t_2 of excess pore pressure dissipation are plotted in Fig. 15 versus impact number for the fully submerged C1 specimen. The dissipation rate of excess pore pressure changes significantly across the solidification front.

The solidification front rises from the bottom as the grains sink. The smaller the change in void ratio caused by liquefaction, the shorter the sedimentation distance and the faster the solidification front rises through the soil bed. The velocity of the solidification front V_{front} can be calculated form the excess pore pressure dissipation start time t_1 and the pore pressure transducer elevation z (Scott 1986; Tsurumi et al. 2000; Kokusho and Kojima 2002)

$$[4] \qquad V_{\mathrm{front}} = \frac{Z}{t_1}$$

The average velocity of the solidification front V_{front} versus impact number is plotted in Fig. 16: as the duration of liquefaction decreases with successive impacts due to densification (see Fig. 15), the velocity of the solidification front increases. For different soils, the evolution of liquefaction and excess pore pressure dissipation and resolidification are controlled by permeability as well, as captured in eq. [1].

Response to successive impacts

Figures 7 and 8 show that the fully submerged specimen and even the mixed saturation specimen can attain a zero effective stress condition multiple times when subjected to the same impact energy (Fig. 5; see field results in Youd 1984; Ashford et al. 2004). As the number of impacts increases, the cumulative settlement increases (Fig. 4), the porosity decreases towards a characteristic terminal porosity, the electrical resistance increases (Fig. 6), the shear wave velocity increases (Fig. 13), and the upwards velocity of the solidification front increases (Fig. 16). On the other hand, the dissipation time for the excess pore pressure decreases with successive events (Fig. 15). All these changes occur with decreasing rate reaching asymptotic values of the corresponding parameters.

Summary and conclusions

The following observations made in this small-scale 1*g* model study are expected to hold at field scales:

(1) High frequency excitation requires high acceleration to cause liquefaction.
(2) While the liquefaction resistance increases in unsaturated sands, liquefaction may still take place in unsaturated soils.
(3) Liquefaction may take place multiple times for equal energy events. The size of the liquefied zone decreases with increasing number of events.
(4) Electrical resistivity profiles reveal not only the densification of the soil specimen but its homogenization with successive liquefaction events.
(5) The time scale for the dissipation of excess pore pressure reflects resedimentation, hydraulic conductivity, unsaturated flow, and drainage conditions. Therefore, pressure diffusion curves may exhibit more than one stage. The duration of liquefaction can outlast the duration of the seismic event in sandy soils.
(6) High repetition rate S-wave transillumination permits insightful monitoring of short-duration events in soils. S-wave propagation data during a liquefaction event show the vanishing of shear stiffness immediately after the event and its gradual recovery afterwards.
(7) The evolution of shear wave propagation velocity and attenuation parallel the time history of excess pore pressure as both wave parameters depend on effective stress in hard-grain soils.
(8) Shear wave propagation and signal detection require a minimum effective stress; consequently, the r_{u} value when S-wave signals are first detected is not constant

Fig. 14. Excess pore pressure head versus shear wave after impact Nos. 8 and 40. Fully submerged C1 specimen. (*a*) Excess pore pressure head at the bottom. (*b*) Shear wave velocity V_S at the bottom. (*c*) Relative shear wave amplitude A_S at the bottom bender element.

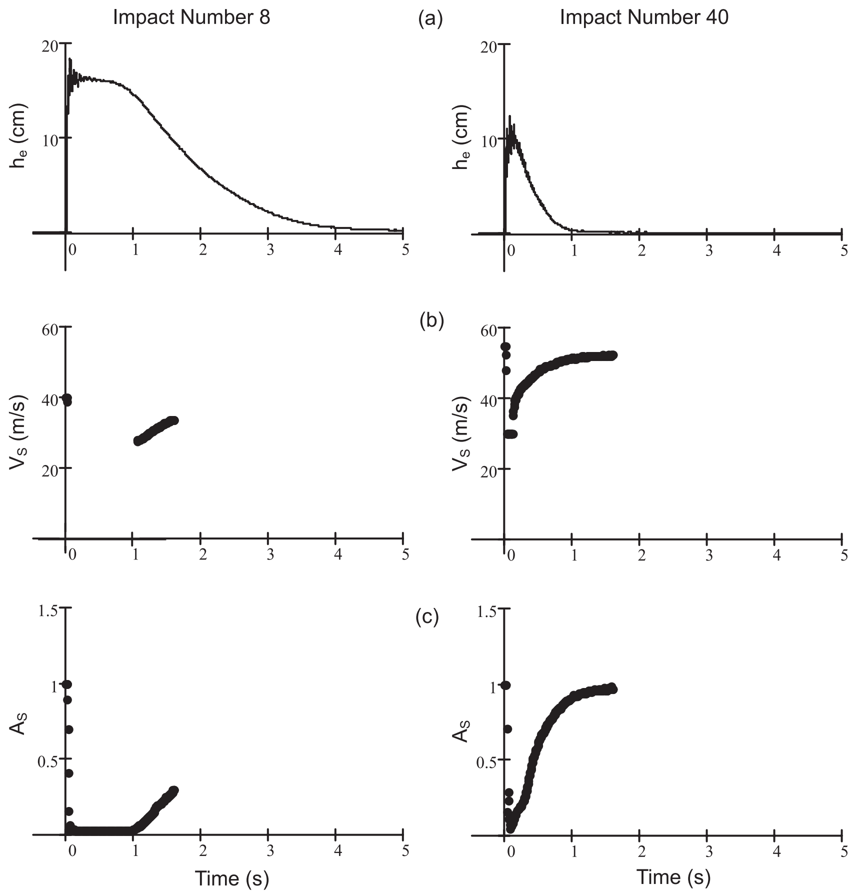

Fig. 15. Start time t_1 and end time t_2 of excess pore pressure dissipation. Fully submerged C1 specimen. See Fig. 7.

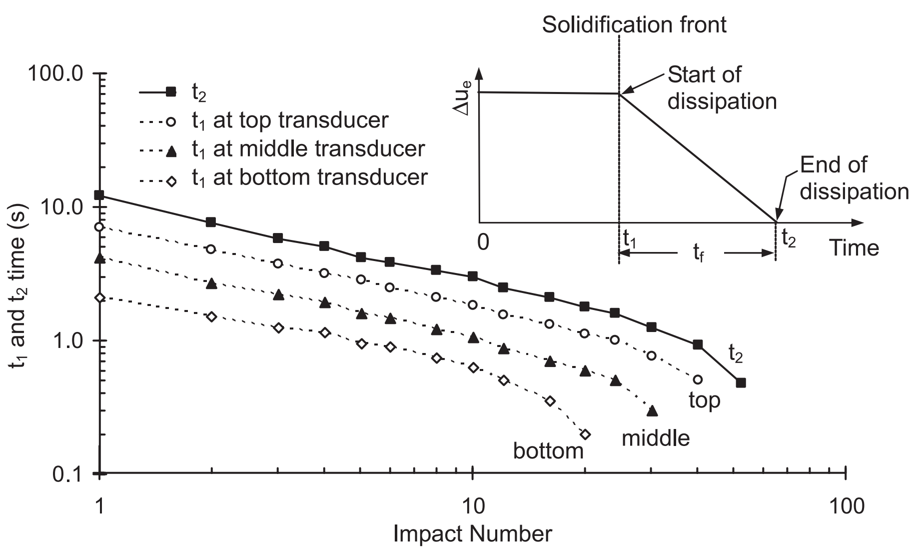

but decreases towards the soil surface. The velocity and amplitude of S-wave signals recover faster at the bottom of the soil column than at the top, confirming that the upward migration of the excess pore water in saturated specimens can cause and (or) sustain zero effective stress conditions in shallow layers.

Fig. 16. Velocity of solidification front V_{front} versus impact number. Fully submerged C1 specimen.

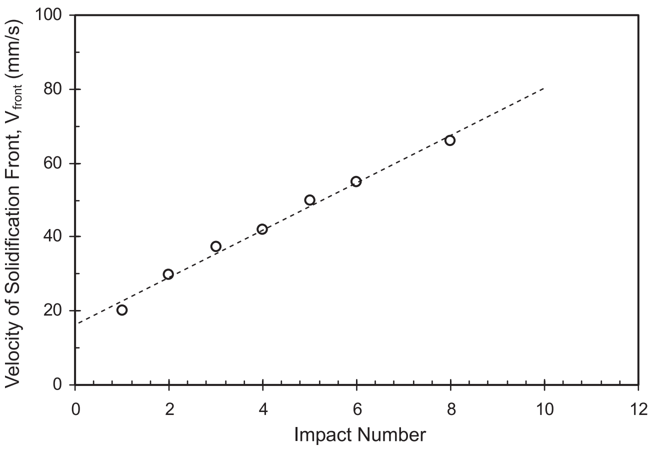

Acknowledgements

This study was supported by the NSF-NEES project (based at the University of California at Davis and directed by Dr. B.L. Kutter), the NSF Mid-America Earthquake Center, and The Goizueta Foundation.

References

Adalier, K., and Elgamal, A.W. 2002. Seismic response of adjacent dense and loose saturated sand columns. Soil Dynamics and Earthquake Engineering, **22**: 115–127.

Alarcon-Guzman, A., Leonards, G.A., and Chameau, J.L. 1988. Undrained monotonic and cyclic strength of sands. Journal of Geotechnical Engineering, ASCE, **114**(10): 1089–1109.

Arulanandan, K., and Scott, R.F. 1993. Project VELACS – control test results. Journal of Geotechnical Engineering, ASCE, **119**(8): 1276–1292.

Ashford, S.A., Rollins, K.M., and Lane, J.D. 2004. Blast-induced liquefaction for full-scale foundation testing. Journal of Geotechnical and Geoenvironmental Engineering, ASCE, **130**(8): 798–806.

Cascante, G., and Santamarina, J.C. 1996. Interparticle contact behavior and wave propagation. Journal of Geotechnical Engineering, ASCE, **122**(10): 831–839.

Cho, G.C., Lee, J.S., and Santamarina, J.C. 2004. Spatial variability in soils: high resolution assessment with electrical needle probe. Journal of Geotechnical and Geoenvironmental Engineering, ASCE, **130**(8): 843–850.

Fiegel, G.L., and Kutter, B.L. 1994. Liquefaction mechanism for layered soils. Journal of Geotechnical Engineering, ASCE, **120**(4): 737–755.

Florin, V.A., and Ivanov, P.L. 1961. Liquefaction of saturated sandy soils. *In* Proceedings of the 5th International Conference on Soil Mechanics and Foundation Engineering, Paris, 17–22 July 1961, pp. 107–111.

Gibson, A.D. 1997. Physical scale modeling of geotechnical structures at one-G. Ph.D. thesis, Department of Civil Engineering, California Institute of Technology, Pasadena, Calif.

Iai, S. 1989. Similitude for shaking table tests on soil-structure-fluid model in 1g gravitational field. Soils and Foundations, **29**(1): 105–119.

Ishihara, K. 1996. Soil behaviour in earthquake geotechnics. Oxford Science Publications, Oxford.

Ishihara, K., Huang, Y., and Tsuchiya, H. 1998. Liquefaction resistance of nearly saturated sand as correlated with longitudinal wave velocity. *In* Proceedings of the Boit Conference on Poromechanics, Poromechanics – a Tribute to Maurice A. Biot. Belgium. A.A. Balkema, the Netherlands. pp. 583–586.

Ishihara, K., Muroi, T., and Towhata, I. 1989. In-situ pore-water pressures and ground motions during the 1987 Chiba-Toho-Oki earthquake. Soils and Foundations, **29**(4): 75–90.

Knox, D.P., Stokoe II, K.H., and Kopperman, S.E. 1982. Effect of state of stress on velocity of low-amplitude shear waves propagating along principal stress directions in dry sand. Geotechnical Engineering Report GR 82-23, University of Texas at Austin.

Kokusho, T. 1999. Water film in liquefied sand and its effect on lateral spread. Journal of Geotechnical and Geoenvironmental Engineering, ASCE, **125**(10): 817–826.

Kokusho, T. 2003. Current state of research on flow failure considering void redistribution in liquefied deposits. Soil Dynamics and Earthquake Engineering, **23**: 586–603.

Kokusho, T., and Kojima, T. 2002. Mechanism for postliquefaction water film generation in layered sand. Journal of Geotechnical and Geoenvironmental Engineering, ASCE, **128**(2): 129–137.

Krammer, S.L. 1996. Geotechnical earthquake engineering. Prentice Hall, N.J.

Lee, J.S. 2003. High resolution geophysical techniques for small-scale soil model testing. Ph.D. thesis. Department of Civil and Environmental Engineering, Georgia Institute of Technology, Atlanta, Ga.

Park, Y.H. 2001. Study on modeling of excess pore pressure dissipation after liquefaction and liquefaction remediation methods using 1-g shaking table tests. Ph.D. thesis. Department of Civil and Environmental Engineering, Seoul National University, Seoul, Korea.

Poorooshasb, H.B. 1995. One gravity model testing. Soils and Foundations, **35**(3): 55–59.

Rocha, M. 1957. The possibility of solving soil mechanics problems by the use of models. *In* Proceedings of the 4th International Conference on Soil Mechanics and Foundation Engineering, London, 12–24 August 1957. pp. 183–188.

Roesler, S.K. 1979. Anisotropic shear modulus due to stress anisotropy. Journal of Geotechnical Engineering, ASCE, **105**(7): 871–880.

Santamarina, J.C., Klein, K.A., and Fam, M.A. 2001. Soils and waves particulate materials behavior, characterization and process monitoring. John Wiley & Sons, N.Y.

Schofield, A.N. 1981. Dynamic and earthquake geotechnical centrifuge modeling. *In* Recent advances in geotechnical earthquake engineering and soil dynamics. Rolla, Missouri, 26 April – 3 May 1981. pp. 1081–1100.

Scott, R.F. 1986. Solidification and consolidation of a liquefied sand column. Soils and Foundations, **26**(4): 23–31.

Seed, H.B. 1979. Soil liquefaction and cyclic mobility evaluation for level ground during earthquakes. Journal of Geotechnical Engineering, ASCE, **105**(2): 201–255.

Seed, H.B., and Lee, K.L. 1966. Liquefaction of saturated sands during cyclic loading. Journal of the Soil Mechanics and Foundations Division, ASCE, **92**(6): 105–134.

Tang, H.T. 1987. Large-scale soil structure interaction. Rep. No. NP-5513-SR, Electric Power Research Institute, Palo Alto, Calif.

Tsurumi, T., Mizumoto, K., and Okada, S. 2000. Experimental consideration on the mechanism of liquefaction. *In* Proceedings of the 12th World Conference on Earthquake Engineering, Auckland, New Zealand, 30 January – 4 February 2000. Paper No. 2405.

Vaid, Y.P., and Sivathayalan, S. 2000. Fundamental factors affecting liquefaction susceptibility of sands. Canadian Geotechnical Journal, **37**(3): 592–606.

Youd, T.L. 1984. Recurrence of liquefaction at the same site. *In* Proceedings of the 8th World Conference on Earthquake Engineering, San Francisco, Calif., July 1984. pp. 231–238.

Youd, T.L., and Bennett, M.J. 1983. Liquefaction sites, Imperial Valley, California. Journal of Geotechnical Engineering, ASCE, **109**(3): 440–457.

Youd, T.L., and Holzer, T.L. 1994. Piezometer performance at Wildlife liquefaction site, California. Journal of Geotechnical Engineering, ASCE, **120**(6): 975–995.

Youd, T.L., Idriss, I.M., Andrus, R.D., Arango, I., Castro, G., Christian, J.T., Dobry, R., Finn, W.D.L., Harder, L.F., Hynes, M.E., Ishihara, K., Koester, J.P., Liao, S.S.C., Marcuson III, W.F., Martin, G.R., Mitchell, J.K., Moriwaki, Y., Power, M.S., Robertson, P.K., Seed, R.B., and Stokoe II, K.H. 2001. Liquefaction resistance of soils: summary report from the 1996 NCEER and 1998 NCEER/NSF workshops on evaluation of liquefaction resistance of soil. Journal of Geotechnical and Geoenvironmental Engineering, ASCE, **127**(10): 817–833.

Yu, P., and Richart Jr., F.E., 1984. Stress ratio effects on shear modulus of dry sands. Journal of Geotechnical Engineering, ASCE, **110**(3): 331–345.

Zeghal, M., and Elgamal, A.W. 1994. Analysis of site liquefaction using earthquake records. Journal of Geotechnical Engineering, ASCE, **120**(6): 996–1017.

Zeghal, M., Elgamal, A.W., Tang, H.T., and Stepp, J.C. 1995. Lotung downhole array. II: Evaluation of soil nonlinear properties. Journal of Geotechnical Engineering, ASCE, **121**(4): 363–378.